Combinations of Clinical Factors, CT Signs, and Radiomics for Differentiating High-density Areas After Mechanical Thrombectomy in Patients with Acute Ischemic Stroke

Duchang Zhai*, Yuanyuan Wu*, Manman Cui, Yan Liu, Xiuzhi Zhou, Dongliang Hu, Yuancheng Wang, Shenghong Ju, Guohua Fan, Wu Cai

ABSTRACT

BACKGROUND AND PURPOSE: Clinically, hemorrhagic transformation (HT) after mechanical thrombectomy (MT) is a common complication. This study is aim to investigate the value of clinical factors, CT signs, and radiomics in the differential diagnosis of high-density areas (HDAs) in the brain after MT in patients with acute ischemic stroke with large vessel occlusion (AIS-LVO).

MATERIALS AND METHODS: A total of 156 eligible patients with AIS-LVO in Center I from December 2015 to June 2023 were retrospectively enrolled and randomly divided into training (n=109) and internal validation (n=47) sets at a ratio of 7:3. The data of 63 patients in Center II were collected as an external validation set. According to the diagnostic criteria, the patients in the three datasets were divided into a HT group and a non-HT group. The clinical and imaging data from Centers I and II were used to construct a clinical factor and CT-sign model, a radiomic model and a combined model by logistic regression (LR). Receiver operating characteristic (ROC) analysis was used to evaluate the diagnostic efficacy of each model in the three datasets.

RESULTS: Clinical blood glucose (Glu) and the maximum cross-sectional area ($Area_{max}$) on CT were associated with the nature of the HDA according to multivariate LR analyses ($P < 0.05$). Among the three models, the combined model had the highest diagnostic efficiency, with area under the curve (AUC) values of 0.895, 0.882, and 0.820 in the three datasets, which were significantly greater than the AUC values of the radiomic model (0.887, 0.898, 0.798) and clinical factor and CT sign model (0.831, 0.744, 0.684).

CONCLUSIONS: The combined model based on radiomics had the best performance, indicating that radiomic features can be used as imaging biomarkers to aid in the clinical judgment of the nature of HDA after MT.

ABBREVIATIONS: HDA =high-density area; HT =hemorrhagic transformation; MT =mechanical thrombectomy; AIS-LVO =acute ischemic stroke with large vessel occlusion; LR =logistic regression; AUC =area under the curve; ICE =iodine contrast extravasation; DECT =dual energy CT; IOM =iodine overlay map; VNC =virtual noncontrast; Glu = glucose; LASSO = least absolute shrinkage and selection operator; ICC = intraclass correlation coefficient; ROC =receiver operating characteristic; DCA =decision curve analysis

* These authors contributed equally to this work.

Received month day, year; accepted after revision month day, year.
From the Department of Radiology, The Second Affiliated Hospital of Soochow University, San Xiang Road No. 1055, Suzhou, Jiangsu, 215004, China (D.Z., Y.W., M.C., Y.L., X.Z., D.H., G.F., W.C.); Department of Radiology, Zhongda Hospital, Medical School of Southeast University, Ding Jia Qiao Road No. 87, Nanjing, Jiangsu, 210009, China (Y.W., S.J.).

Please address correspondence to Wu Cai, MD, PhD, Department of Radiology, The Second Affiliated Hospital of Soochow University, San Xiang Road No. 1055, Suzhou, Jiangsu, 215004, China; e-mail: xwg608@126.com

Disclosure
The authors declare no conflicts of interest related to the content of this article.

SUMMARY SECTION

PREVIOUS LITERATURE: AIS-LVO is a highly prevalent and lethal disease, and the most common treatment is MT if the patient is still within the time window. However, the occurrence of HT after MT is a clinical problem of great concern to radiology, neurology and neurosurgery. It is currently difficult to achieve early diagnosis of HDA in the brain after MT without DECT. Therefore radiomics may be helpful in determining the nature of HDA.

KEY FINDINGS: Clinical factors & CT signs & Radiomics model has a good diagnostic efficacy for HT within HDA after MT, and external validation has confirmed this. Thus, radiomics offers a reference for clinical practice and assisting in early treatment decisions.

KNOWLEDGE ADVANCEMENT: Radiomics is able to detect subtle changes in HDA density between HT and ICE, which is difficult for the human eye to do. Combined with clinical and imaging data, we believe that many clinical problems caused by HDA can be solved.

INTRODUCTION

Acute ischemic stroke with large vessel occlusion (AIS-LVO) is a serious form of AIS with a dire prognosis and is associated with staggering disability and a mortality rate surpassing 70%.[1] At present, mechanical thrombectomy (MT) is the preferred therapeutic method for patients with AIS-LVO.[2] In the pursuit of averting postoperative complications, NCCT post-MT has emerged as an indicator of potential complications. The high-density area (HDA) within the cerebral parenchyma is a frequent radiological discovery with an incidence of 73%, which can stem from iodine contrast extravasation (ICE) during MT or incipient hemorrhagic transformation (HT).[3] Differentiating between these two imaging methods on CT alone is difficult, and multiple postoperative CT reviews are required for differentiation. However, there is a large difference in the methods used for clinical intervention. Current investigations predominantly focus on effectively extracting CT image features, such as the maximum CT value of HDA and the metallic hyperdensity sign, to distinguish between them. [4] In recent years, dual energy CT (DECT) has been a breakthrough in the early differential diagnosis of HT and ICE, which uses two different energy levels to organize material qualitative and quantitative analysis, produce different types of images, such as Z-effective, iodine overlay map (IOM), virtual noncontrast (VNC) and so on. Due to the different attenuation characteristics of iodine and blood, two specific energy levels (generally 80 keV and 140 keV) can be used to distinguish HT from ICE. Therefore, some studies have suggested that DECT is the gold standard to distinguish the two. However, DECT equipment is relatively expensive and currently has a low penetration rate, which largely limits the application of DECT in the differential diagnosis of the two.[5] Therefore, the results of multiple follow-up visits after MT are still used as the diagnostic criteria in clinical practice.

Nevertheless, conventional imaging feature diagnosis relies heavily on the experience of radiologists and often falls short in precise quantitative assessments. Presently, radiomics is a frontier driven by quantitative evaluation, the application of which enriches our understanding of intracranial diseases, such as brain tumors, spontaneous or traumatic hematomas, aneurysms, and neurological function.[6-10] Therefore, radiomic quantitative evaluation can theoretically be applied to enhance differentiating capabilities between HT and ICE.

However, there are few reports on the application of radiomics in the differential diagnosis of HDA, and external validation is lacking. Accordingly, this study endeavored to explore the utility of clinical factors, CT signs, and radiomics in identifying HDA post-MT in AIS-LVO patients.

MATERIALS AND METHODS

Study Patients

The study received ethics committee approval, and informed consent was waived. A total of 431 patients with AIS-LVO who underwent MT at our hospital (Center I) and 188 patients at another hospital (Center II) from December 2015 to June 2023 were retrospectively collected. Patients were required to meet the following criteria: 1) had an AIS-LVO diagnosis by clinical and imaging examination; 2) had MT treatment performed within 12 hours after admission; 3) had a new-onset HDA underwent NCCT scan within 1 hour after MT; 4) had a brain NCCT scan ≥2 times within 48 hours after MT. In addition, we excluded patients (n=275 in Center I, n=125 in II) for the following reasons: the absence of new HDA on NCCT scans (n=247 in Center I, n=108 in II); fewer than 2 postoperative CT reviews 24-48 hours (n=23 in Center I, n=15 in II); the presence of HDA (such as hemorrhage or calcification) in the corresponding region of the brain before MT (n=3 in Center I, n=1 in II); and incomplete clinical and imaging data (n=2 in Center I, n=1 in II). We employed an accepted approach to differentiate HT from ICE. For cases where the HDA had diminished or entirely dissipated within 48 hours, which was considered to the simple ICE (non-HT). In contrast, persistent or enlarged HDA was considered to indicate HT. DECT can also be used as a valuable reference standard, if available. The diagnostic criteria were as follows: HDA was present on both the original image and VNC image; however, when the range of HDA in the corresponding region was reduced or disappeared on IOM image, HT was considered. However, when HDA was present on the original image and IOM image but not in the corresponding region on the VNC image, ICE was considered.[11] Finally, 156 patients in Center I were selected and split into a training cohort (66 males, 43 females, average age 63.93±14.05 years) and an internal validation cohort (25 males, 22 females, average age 63.72±14.23 years). Sixty-three patients in Center II composed the external validation cohort. Patients were categorized into an HT group and a non-HT group based on diagnostic criteria. The flow chart of patient enrollment is shown in Fig 1.

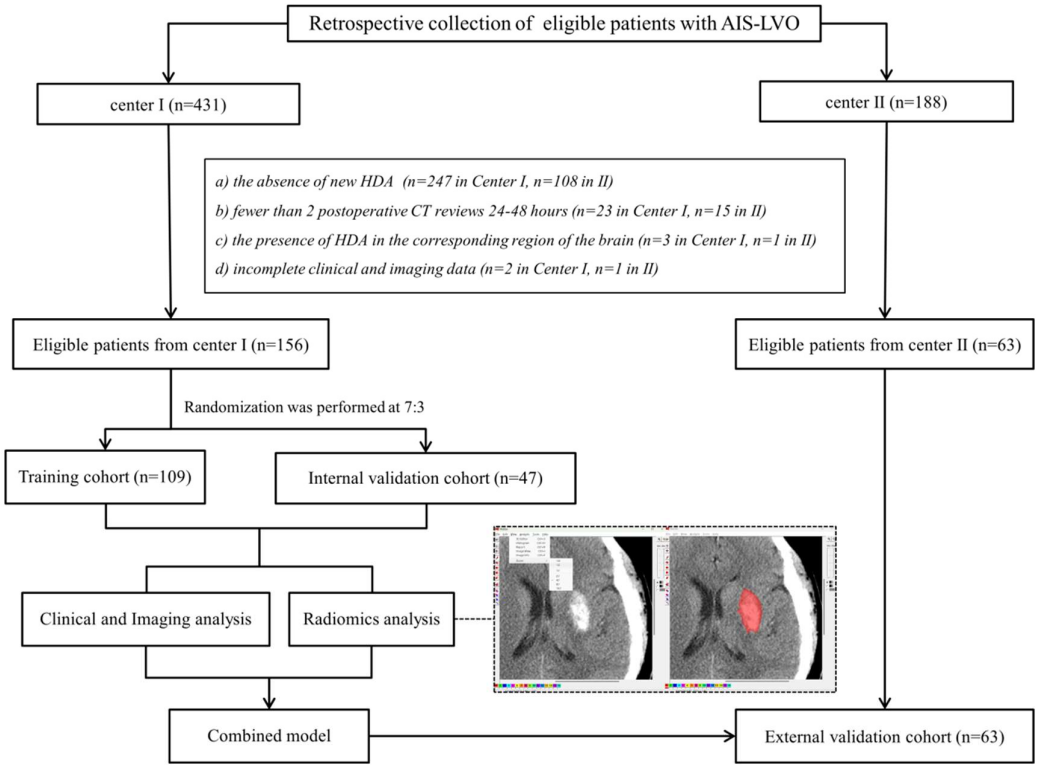

FIG 1. Flow chart of the grouping of the included patients and model building.

Clinical and Imaging Data Collection

The clinical medical records and picture archiving and communication systems (PACSs) of Center I and Center II were consulted. Laboratory data (platelet (PLT), prothrombin time (PT), thrombin time (TT), antithrombin-III (AT-III), activated partial thromboplastin time (APTT), D-dimer (D-D), fibrinogen (FIB), international normalized ratio (INR), low-density lipoprotein (LDL), total cholesterol (TC), triglyceride (TG), glucose (Glu), medical history (age, sex, hypertension, smoking status, alcohol, cerebral infarction, cerebral hemorrhage, embolism of cardiac origin, intravenous thrombolysis, anticoagulant therapy), clinical records pertaining to MT treatment, systolic blood pressure (SBP), Glasgow Coma Scale (GCS), National Institutes of Health Stroke Scale (NIHSS), door-to-puncture (DPT), location of the MT, Times, Stent, mTICI and initial postoperative NCCT scans (location of HDA, maximum CT value, mean CT value, the maximum cross-sectional area ($Area_{max}$), high-density lesions in the subarachnoid space, mass effect, low-density edema zone, low-density mixed sign, metallic hyperdensity sign) were collected. The scanning scope extended from the skull base to the cranial apex. The following scanning parameters were used: 64-slice spiral CT (Discovery CT 750 HD, GE Healthcare); tube voltage, 120 kV; tube current, 300 mAs; and slice thickness, 5 mm. When two HDAs were present in a patient, the one with the largest area was selected for analysis. The CT signs of the enrolled patients were evaluated by two radiologists, A and B, who had 5 years of experience each, and the final diagnosis was made by Radiologist C, who had 10 years of experience when radiologists A and B disagreed. In the training set of Center I, through univariate and multivariate logistic regression (LR) analyses, the

clinical factors and CT signs with $P<0.05$ were incorporated into a subset, and a clinical factor and CT sign model was established.

Radiomics data collection

Image preprocessing and initial texture feature extraction

The initial postoperative NCCT scans of our patient cohort were meticulously evaluated within the PACS system at Center I and Center II. DICOM-formatted images of the largest HDA cross-section were exported and processed using Mazda software (version 4.6, http://www.eletel.p.lodz.pl/mazda/). After the image was loaded, we normalized it with the $\mu\pm3\sigma$ method (μ is the mean value of the image gray value, and σ is the standard deviation of the image gray value) to reduce contrast and brightness fluctuations. The default ROI was cleared, and 4× magnification was applied. The ROI was meticulously delineated around the HDA contours (Fig 1), and initial texture features were obtained. We randomly selected 30 patients, and two radiologists (A and B) independently performed ROI segmentation and feature extraction. Radiologist A repeated the process after one month to assess interobserver agreement.

Feature selection and model establishment

In this study, we employed MaZda software to extract a comprehensive set of 279 texture features belonging to 6 types from all the ROIs of the training set of Center I. To refine our feature selection process for discriminating the nature of HDA, we implemented the least absolute shrinkage and selection operator (LASSO) regression algorithm and performed a significance analysis. Subsequently, the optimal feature subset was incorporated into a LR model to construct the radiomic model. This radiomic model was then integrated with clinical factors and CT signs via LR to construct the combined model.

Interobserver consistency analysis of radiomics

30 patients were randomly selected from the enrolled patients, and the ROI segmentation and initial texture feature extraction of HDA were independently completed by radiologists A and B. After an interval of 1 month, the ROI was outlined again by radiologist A for these 30 patients.[12] The intraclass correlation coefficient (ICC) of features extracted by two radiologists ranged from 0.787-0.945, and the ICC of features extracted by radiologist A twice independently ranged from 0.838-0.997. These findings demonstrated good consistency in terms of feature extraction. Subsequently, Radiologist A autonomously performed ROI segmentation and initial texture feature extraction for the remaining patients.

Statistical analysis

SPSS software version 26.0 and R Studio software version 4.2.0 were used for statistical analysis. The receiver operating characteristic (ROC) curve was used to evaluate the diagnostic efficacy of the model in three datasets (training set, internal validation set and external validation set). The metrics assessed included the area under the curve (AUC), sensitivity (SEN), specificity (SPE), and accuracy (ACC). The DeLong test was used to compare the diagnostic efficacy of the three models. The clinical practicability of the model was elucidated via decision curve

analysis (DCA), which offered insights into net benefit variations with threshold probability changes. Finally, the model was visualized as a nomogram. $P<0.05$ was considered to indicate statistical significance.

RESULTS

Clinical factors and CT signs model

In the training set of Center I, the patients were divided into two groups (HT, n=50; non-HT, n=59) according to the diagnostic criteria. There were significant differences in clinical data encompassing the PLT, D-D, TG, cardiogenic embolism, Glu, admission NIHSS score, DPT, and stent between the two groups ($P<0.05$). According to the included imaging data, there were statistically significant differences between the two groups ($P<0.05$) in the $Area_{max}$ of HDA, the high density subarachnoid space, the mass effect, the low density edema zone, and the low density mixed sign. In Online Supplemental Data:, comprehensive statistical findings are presented. Univariate and multivariate LR analyses in the training cohort revealed significant differences in Glu and $Area_{max}$ levels ($P<0.05$), as shown in Table 1. After incorporating two independent risk factors, we constructed a model of clinical factors and CT signs. Testing and validation were performed in the internal validation set and the external validation set. ROC curve analysis (Fig 2, Fig 3A) demonstrated the good discriminative performance of the clinical factors and CT signs model, yielding AUC of 0.831 (95% CI 0.756-0.905), 0.744 (95% CI 0.597-0.892), and 0.684 (95% CI 0.542-0.825) across the three datasets. Brier scores approaching 0 across all three datasets indicate that the clinical factor and CT sign models had robust discrimination and calibration ability. Online Supplemental Data: provides a comprehensive overview of the diagnostic efficacy of three models. Fig 3B shows the DCA results for the external validation set.

Radiomics model and combined model

Initial texture feature dimension reduction, selection and model establishment

In this study, we employed the significance analysis method and LASSO regression to condense the initial 279 texture features across 6 categories, which were extracted using Mazda software from ROIs of the training set of Center I. Through tenfold cross-validation, we identified 2 vital features, S(0,4)SumAverg and 45dgr_GLevNonU, which were incorporated into the optimal feature set (Fig 4).

Diagnostic value of the radiomic model and combined model

In the training set, the optimal feature set was used to perform LR and construct the radiomic model and the combined model. Utilizing R Studio 4.2.0 software, the calculations demonstrated that the combined model exhibited superior diagnostic efficiency, with an impressive AUC of 0.895 (95% CI 0.833-0.956), 0.882 (95% CI 0.773-0.990), and 0.820 (95% CI 0.689-0.952) across the three datasets. In comparison, the radiomic model also demonstrated commendable AUC of 0.887 (95% CI 0.824-0.957), 0.898 (95% CI 0.801-0.996), and 0.798 (95% CI 0.655-0.940) in the three datasets. According to the DeLong test, the diagnostic efficacy of the AUC of the combined model and the clinical factor and CT sign models were significantly different among the three datasets (training set $P=0.018$, internal validation set $P=0.038$, external validation set $P=0.044$). There were no statistically significant differences between the combined model and the radiomics model in any of the three datasets (all $P>0.05$). In the internal validation set, the AUC of the radiomic model was significantly greater than that of the clinical factor and CT-sign

model (*P*=0.030). These findings underscore that radiomics features can further significantly improve diagnostic performance on the basis of the clinical factor and CT sign models, as summarized in Table 2.

The Brier scores revealed close-to-zero values for both the radiomic model and the combined model across the three datasets, indicating strong discrimination, calibration, repeatability, and extrapolation capabilities. Notably, both models exhibited superior sensitivity and accuracy compared to those of the clinical factor and CT sign models (Online Supplemental Data:).

The DCA results of the three models in the external validation set are shown in Fig 3B. Our findings clearly demonstrate that the combined model outperforms the other models in diagnosing HDA with HT, particularly at a threshold probability range of 16%-44%, indicating that its clinical practical value is the highest. The ROC curves of the three models in the three datasets are shown in Fig 2, and the AUC values are visualized as bar charts for easy comparison (Fig 3A). Among the three models, the combined model had the highest diagnostic efficiency; therefore, a nomogram was drawn (Fig 3C).

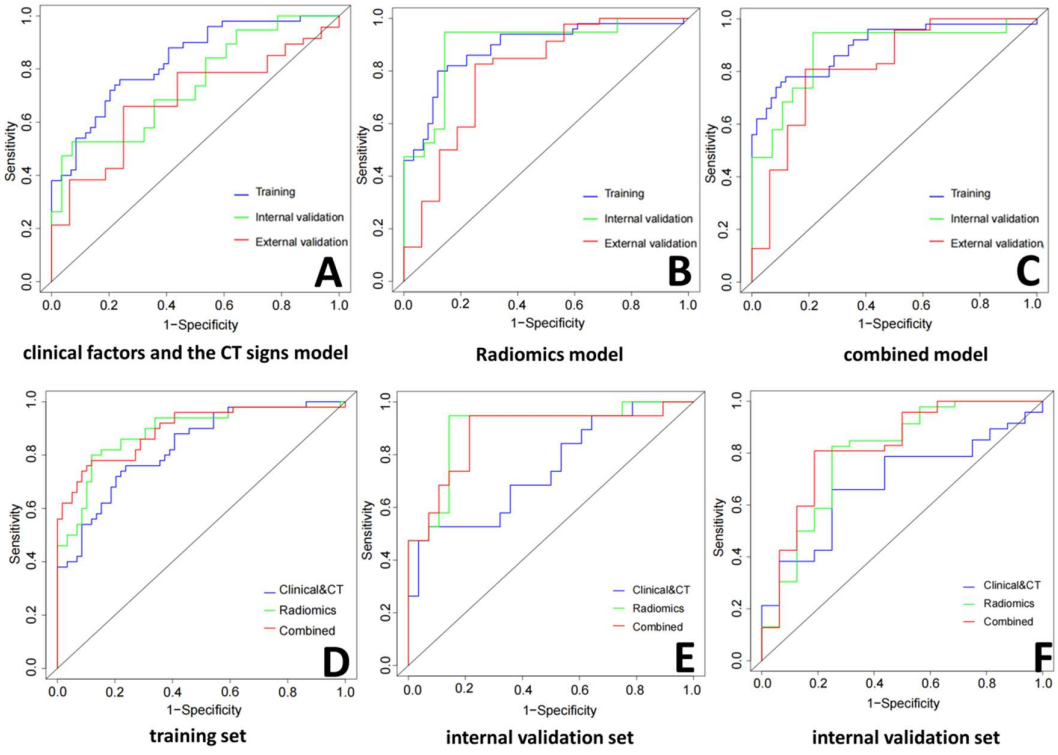

FIG 2. A-F: ROC curves of clinical factors and the CT signs model, Radiomics model and combined model in the training set, internal validation set and external validation set.

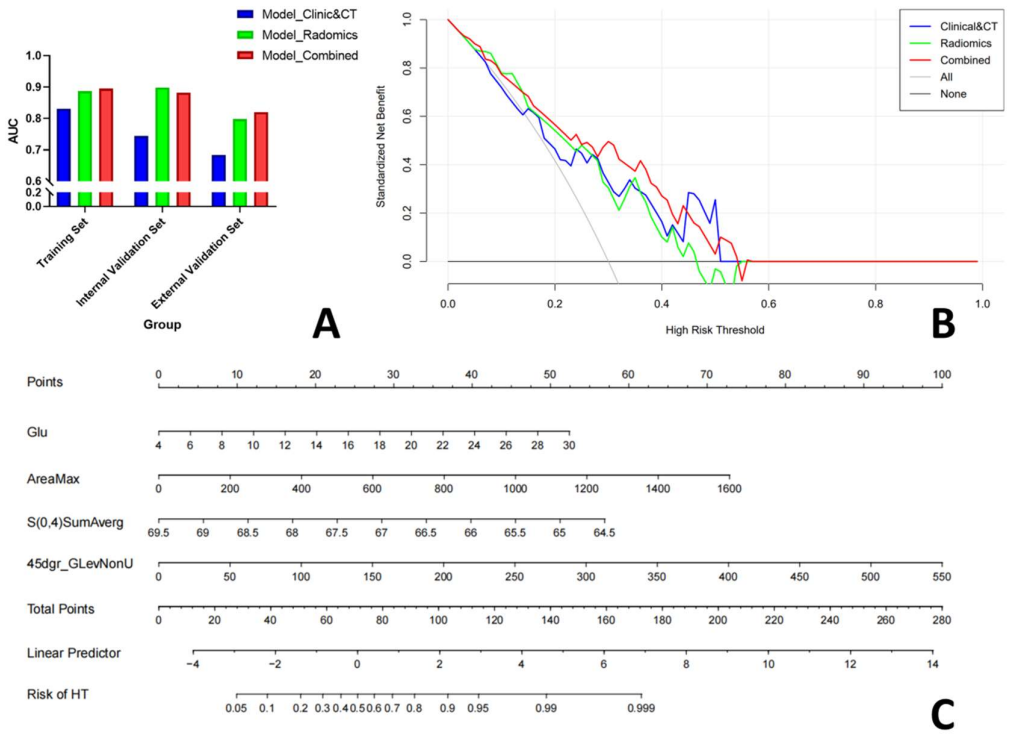

FIG 3. A: The AUC values of the three models are visualized as bar graphs; B: DCA curves of clinical factors and the CT signature model, radiomics model, and combined model in the external validation set; C: Nomogram of the combined model.

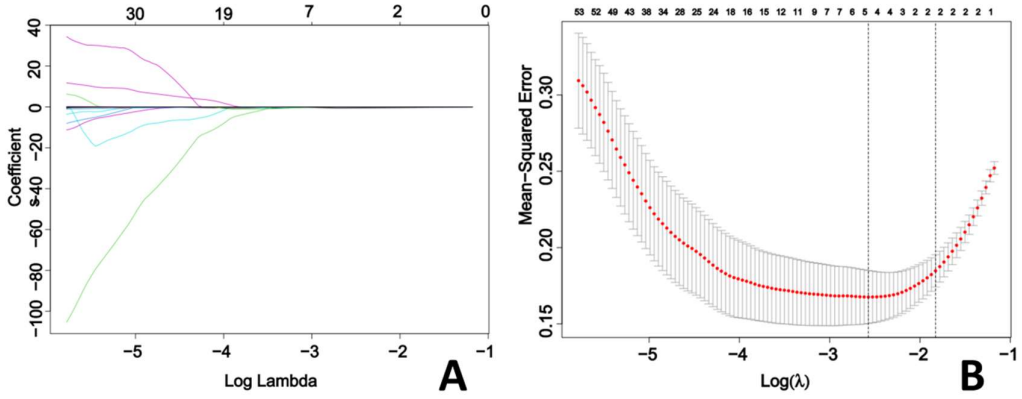

FIG 4. A-B: LASSO regression and significance analysis are used to refine the optimal features.

DISCUSSION

At present, the clinical judgment of the nature of HDA is mostly based on the subjective evaluation of postoperative brain NCCT images[13], which is highly variability due to radiologists' experience. With the precision of radiomics in overcoming the uncertainty of human subjective judgment, this study aimed to establish a clinical factor and CT sign model, a radiomic model, and a combined model. A comparative evaluation of the diagnostic efficacy of the three models, alongside external validation (Center II), verified their stability and applicability.

To enable early identification of simple ICE and intraparenchymal hemorrhage (IPH) following MT, Chen et al.[14] pioneered the classification of simple and mixed contrast hemorrhages as IPH, a method adopted in our study. The Rad-score exhibited robust performance, with impressive AUC values of 0.848 and 0.826 in the training and validation cohorts, respectively. However, our novel radiomic model, which leverages NCCT scans, outperformed Chen's model, with AUC values of 0.887 (training set) and 0.898 (internal validation set). The introduction of clinical risk factors further enhanced diagnostic efficacy, achieving AUC values of 0.895 (training set) and 0.882 (internal validation set). Remarkably, external validation in Center II reaffirmed our combined model's robustness, with an AUC of 0.820, attesting to its high diagnostic efficiency, generalizability, and stability.

Similarly, Ma et al.[15] also conducted a meticulous investigation encompassing clinical, radiomic and combined models on this issue. These findings underscore the commendable performance of the radiomic model in both the training set (AUC=0.955) and the validation set (AUC=0.869), with the combined model exhibiting the disadvantage of diagnostic proficiency (AUC=0.972 in the training set; AUC=0.926 in the validation set). Notably, both models significantly outperformed the clinical factor and CT sign models. However, the sample size of this study was limited (104 patients), which may affect the accuracy, stability and reproducibility of the model; thus, external validation is needed in the future for robust clinical applicability and generalizability. Moreover, a small sample size may also lead to an imbalance between groups and the possibility of overfitting the model. Ma et al.[15] applied 3D measurement methods to segment HDA. While some studies[16] have suggested that 3D analysis provides richer information, others[17] have argued that 2D measurements are more reliable due to potential overfitting with additional layers. Furthermore, the time-consuming layer-by-layer delineation of 3D measurements may impact clinical decision-making in HT diagnosis and intervention.

In this study, LASSO regression and significance analysis were used to refine the initial features. Ultimately, two discriminative features emerged as the focal points of our analysis: S(0,4)SumAverg and 45dgr_GLevNonU. SumAverg denotes the sum of pixel averages in a specific direction, derived from co-occurrence matrix analysis, which reflects the uniformity of tissue density by describing the density change with increasing distance in the ROI, with lower values signifying reduced uniformity.[18, 19] Yue et al. [20] used the Mazda software, and by combining texture features , clinical data and CT features, it was found that S(1,0,0) SumAverg showed good discriminative ability (AUC=0.892) for distinguishing signet-ring cell carcinoma (SRCC) from adenocarcinoma (AC), with higher efficacy than clinical features (AUC=0.745). Conversely, GLevNonU denotes gray level nonuniformity, extracted from the run-length matrix, where the matrix elements are defined as the frequencies that satisfy a particular gray level value in a particular run length. Thus, the feature GLevNonU is a measure of the uniformity of the pixel gray level distribution of the underlying tissue, with elevated values indicative of heightened image heterogeneity, reflecting the heterogeneity of the image in different directions.[21] Li et al [22] performed texture analysis based on CT images to predict whether primary hepatocellular carcinoma has microvascular invasion (MVI), and the results showed that the 45dgr_GLevNonU in the MVI-positive group was significantly higher than that in the MVI-negative group (AUC = 0.762). Remarkably, the S(0,4)SumAverg of the HT group was lower than that of the non-HT group, and the 45dgr_GLevNonU was higher than that of the non-HT group in our study, revealing that HT in HDA, as observed in NCCT images, exhibited diminished uniformity compared to pure ICE. This result

demonstrated that there is more leakage of tangible substances from the blood during the development of HT, thus causing heterogeneity on NCCT images. This nuanced distinction, often elusive to the human eye, underscores the unique advantage of radiomics in quantifying the heterogeneity of HDA density.

This study revealed that a high blood glucose level at admission was an independent risk factor for HT, which was consistent with the results of prior research.[23-25] In a meticulous multicenter randomized controlled trial (RCT) conducted by Tian et al.[26], two pivotal factors, namely, elevated NIHSS scores and heightened admission blood glucose levels, independently emerged as robust predictors of symptomatic intracerebral hemorrhage (sICH). From a pathophysiological perspective, the linkage between hyperglycemia and heightened HT risk after MT can be delineated. As blood glucose levels surge, accelerated anaerobic glycolysis occurs within cells, leading to the accumulation of acidic metabolites. These metabolites, in turn, serve as catalysts for the production of matrix metalloproteinase-9 and subsequent extracellular matrix protein degradation, thereby compromising the integrity of the BBB.[27] This dual-action mechanism escalates BBB permeability, thereby heightening vulnerability to HT. Furthermore, high blood glucose levels may compromise cerebral autoregulatory function, potentially exacerbating reperfusion injury following successful recanalization of MT.[28-30] In light of these findings, the management of blood glucose levels both in daily life and in the perioperative period is imperative for mitigating the risk of postoperative HT in patients with AIS-LVO.

In this study, our multivariate analysis of various CT signs revealed that the $Area_{max}$ of the HDA serves as an independent risk factor for HT. However, our results diverge from those of Portela's research, where no statistically significant difference in the $Area_{max}$ index of HDA was detected between the HT (1561.9 mm^2) and non-HT (1123.7 mm^2) groups.[31] It is worth noting that Portela's study had a limited sample size of 29 patients and lacked validation sets. We conducted internal and external validation based on a larger sample size (AUC=0.792 in the training set; AUC=0.713 in the internal validation set; and AUC=0.642 in the external validation set), and the results showed that the $Area_{max}$ mutation in the HDA was an independent risk factor for HT. However, other studies have suggested that the high diagnostic efficacy of $Area_{max}$ may be attributed to the fact that ICE and HT are different stages of the same pathological process.[32] In minor BBB basement membrane damage, only slight permeability increase occurs, leading to the extravasation of low-molecular-weight substances such as iodinated contrast agents. Conversely, severe damage results in heightened permeability, allowing larger molecular weight substances such as blood constituents to escape into the extravascular space. Gradual accumulation of these larger molecules contributes to the expansion of HDA on CT images.[32] Furthermore, HT-induced vascular rupture or the “avalanche” effect can lead to continuous hemorrhage and hematoma enlargement in the brain parenchyma.[33-35]

While the performance of our study's model is deemed satisfactory, several limitations must be acknowledged. First, this retrospective approach presents inherent constraints, warranting future prospective, large-scale, multicenter RCTs for enhanced evidential support. Second, manual ROI delineation, a time-intensive process prone to fatigue-induced variability among radiologists, was employed. Future investigations should leverage machine learning and AI for efficient, reproducible, and accurate lesion segmentation. Third, the absence of pre-MT medication data and analysis of the impacts of antiplatelet and lipid-lowering drugs limit our conclusions. Fourth, our LR-based model awaits comparison with various machine learning algorithms, including vector machine (SVM),

random forest (RF), linear SVC, adaptive enhancement (AdaBoost), decision tree (DT), and Bayesian algorithms, as well as exploration of deep learning for radiomics with substantial, high-dimensional data.

CONCLUSIONS

In conclusion, among the three models discussed in this study, the combined radiomic model demonstrated superior diagnostic performance. Thus, radiomics has emerged as a valuable imaging biomarker, offering a reference for clinical practice and assisting in early treatment decisions.

ACKNOWLEDGMENTS

None

REFERENCES

1. Li W, Qi Z, Ma Q, et al. Normobaric hyperoxia combined with endovascular treatment for patients with acute ischemic stroke: a randomized controlled clinical trial. *Neurology* 2022;99:e824-e834
2. Powers WJ, Rabinstein AA, Ackerson T, et al. Guidelines for the Early Management of Patients With Acute Ischemic Stroke: 2019 Update to the 2018 Guidelines for the Early Management of Acute Ischemic Stroke: A Guideline for Healthcare Professionals From the American Heart Association/American Stroke Association. *Stroke* 2019;50:e344-e418
3. Leslie-Mazwi T, Chen M, Yi J, et al. Post-thrombectomy management of the ELVO patient: Guidelines from the Society of NeuroInterventional Surgery. *J Neurointerv Surg* 2017;9:1258-1266
4. Xu C, Zhou Y, Zhang R, et al. Metallic hyperdensity sign on noncontrast CT immediately after mechanical thrombectomy predicts parenchymal hemorrhage in patients with acute large-artery occlusion. AJNR Am J Neuroradiol 2019;40:661-667
5. Yedavalli V, Sammet S. Contrast extravasation versus hemorrhage after thrombectomy in patients with acute stroke [J]. *J Neuroimaging,* 2017, 27(6): 570-576.
6. Li Y, Liu Y, Liang Y, et al. Radiomics can differentiate high-grade glioma from brain metastasis: a systematic review and meta-analysis. *Eur Radiol* 2022;32:8039-8051
7. Zhang L, Zhuang Q, Wu G, et al. Combined radiomics model for prediction of hematoma progression and clinical outcome of cerebral contusions in traumatic brain injury. *Neurocrit Care* 2022;36:441-451
8. Lauric A, Ludwig CG, Malek AM. Enhanced radiomics for prediction of rupture status in cerebral aneurysms. *World Neurosurg* 2022;159:e8-e22
9. Kim KM, Hwang H, Sohn B, et al. Development and validation of MRI-based radiomics models for diagnosing juvenile myoclonic epilepsy. *Korean J Radiol* 2022;23:1281-1289
10. Xu X, Zhang J, Yang K, et al. Prognostic prediction of hypertensive intracerebral hemorrhage using CT radiomics and machine learning. *Brain Behav* 2021;11:e02085
11. Hoche C, Henderson A, Ifergan H, et al. Determinants and Clinical Relevance of Iodine Contrast Extravasation after Endovascular Thrombectomy: A Dual-Energy CT Study. *AJNR Am J Neuroradiol.* 2023;45(1):30-36.
12. Zheng Y, Han X, Jia X, et al. Dual-energy CT-based radiomics for predicting invasiveness of lung adenocarcinoma appearing as ground-glass nodules. *Front Oncol.* 2023;13:1208758.
13. Gupta R, Phan CM, Leidecker C, et al. Evaluation of dual-energy CT for differentiating intracerebral hemorrhage from

iodinated contrast material staining. *Radiology* 2010;257:205-211

14. Chen X, Li Y, Zhou Y, et al. CT-based radiomics for differentiating intracranial contrast extravasation from intraparenchymal haemorrhage after mechanical thrombectomy. *Eur Radiol* 2022;32:4771-4779
15. Ma Y, Wang J, Zhang H, et al. A CT-based radiomics nomogram for classification of intraparenchymal hyperdense areas in patients with acute ischemic stroke following mechanical thrombectomy treatment. *Frontiers in Neuroscience* 2023;16:1061745
16. Ng F, Kozarski R, Ganeshan B, et al. Assessment of tumor heterogeneity by CT texture analysis: can the largest cross-sectional area be used as an alternative to whole tumor analysis? *Eur J Radiol* 2013;82:342-348
17. Ahn SJ, Kim JH, Park SJ, et al. Prediction of the therapeutic response after FOLFOX and FOLFIRI treatment for patients with liver metastasis from colorectal cancer using computerized CT texture analysis. *Eur J Radiol* 2016;85:1867-1874
18. Miles KA, Ganeshan B, Griffiths MR, et al. Colorectal cancer: texture analysis of portal phase hepatic CT images as a potential marker of survival. *Radiology* 2009;250:444-452
19. Miles KA, Ganeshan B, Hayball MP. CT texture analysis using the filtration-histogram method: what do the measurements mean? *Cancer Imaging* 2013;13:400-406
20. Yue Y, Hu F, Hu T, et al. Three-dimensional CT texture analysis to differentiate colorectal signet-ring cell carcinoma and adenocarcinoma [J]. *Cancer Manag Res*, 2019, 11: 10445-10453
21. Baessler B, Mannil M, Maintz D, et al. Texture analysis and machine learning of non-contrast T1-weighted MR images in patients with hypertrophic cardiomyopathy-Preliminary results. *Eur J Radiol* 2018;102:61-67
22. Li Y, Xu X, Weng S, et al. CT image-based texture analysis to predict microvascular invasion in primary hepatocellular carcinoma [J]. *J Digit Imaging,* 2020, 33(6): 1365-1375.
23. Gofir A, Mulyono B, Sutarni S. Hyperglycemia as a prognosis predictor of length of stay and functional outcomes in patients with acute ischemic stroke. *Int J Neurosci* 2017;127:923-929
24. Goyal N, Tsivgoulis G, Pandhi A, et al. Admission hyperglycemia and outcomes in large vessel occlusion strokes treated with mechanical thrombectomy. *J Neurointerv Surg* 2018;10:112-117
25. Neuberger U, Kickingereder P, Schönenberger S, et al. Risk factors of intracranial hemorrhage after mechanical thrombectomy of anterior circulation ischemic stroke. *Neuroradiology* 2019;61:461-469
26. Tian B, Tian X, Shi Z, et al. Clinical and imaging indicators of hemorrhagic transformation in acute ischemic stroke after endovascular thrombectomy. *Stroke* 2022;53:1674-1681
27. Mittal R, Patel AP, Debs LH, et al. Intricate functions of matrix metalloproteinases in physiological and pathological conditions. *J Cell Physiol* 2016;231:2599-2621
28. Kruyt ND, Biessels GJ, Devries JH, et al. Hyperglycemia in acute ischemic stroke: pathophysiology and clinical management. *Nat Rev Neurol* 2010;6:145-155
29. Suh SW, Shin BS, Ma H, et al. Glucose and NADPH oxidase drive neuronal superoxide formation in stroke. *Ann Neurol* 2008;64:654-663
30. Martini SR, Kent TA. Hyperglycemia in acute ischemic stroke: a vascular perspective. *J Cereb Blood Flow Metab* 2007;27:435-451
31. Portela de Oliveira E, Chakraborty S, Patel M, et al.Value of high-density sign on CT images after mechanical thrombectomy

for large vessel occlusion in predicting hemorrhage and unfavorable outcome. *Neuroradiol J* 2021;34:120-127

32. Chen Z, Zhang Y, Su Y, et al. Contrast extravasation is predictive of poor clinical outcomes in patients undergoing endovascular therapy for acute ischemic stroke in the anterior circulation. *J Stroke Cerebrovasc Dis* 2020;29:104494
33. Greenberg SM, Nandigam RN, Delgado P, et al. Microbleeds versus macrobleeds: evidence for distinct entities. *Stroke* 2009;40:2382-2386
34. Sarfo FS, Ovbiagele B, Gebregziabher M, et al. Unraveling the risk factors for spontaneous intracerebral hemorrhage among West Africans. *Neurology* 2020;94:e998-e1012
35. Morotti A, Dowlatshahi D, Boulouis G, et al. Predicting intracerebral hemorrhage expansion with noncontrast computed tomography: the BAT score. *Stroke* 2018;49:1163-1169

Table 1 Multivariate LR analysis of clinical factors and CT signs in the training cohort

Factors	*P value*	OR(95%CI)
PLT(10^9/L)	0.122	0.99(0.98-1.00)
D-D(μg/ml)	0.418	1.07(0.90-1.29)
TG(mmol/L)	0.822	0.91(0.35-1.89)
Embolism of cardiac origin	0.378	1.75(0.51-6.36)
Glu(mmol/L)	**0.029***	1.26(1.05-1.58)
NIHSS	0.826	1.01(0.88-1.17)
DPT(min)	0.704	1.00(0.99-1.00)
Stent	0.151	0.18(0.01-1.38)
$Area_{max}$ (mm^2)	**0.006***	1.00(1.00-1.01)
High-density lesions in the subarachnoid space	0.582	0.71(0.20-2.33)
Mass effect	0.080	4.00(0.90-21.35)
Low density edema zone	0.220	2.67(0.58-14.29)
Low density mixed sign	0.944	0.96(0.29-3.09)

* P <0.05 is considered to indicate statistical significance.

Table 2 Statistical differences in the AUC values of the three models

Datasets	clinical factors & CT signs model/Radiomics model	Radiomics model/Combined model	clinical factors & CT signs model/Combined model
Training set	0.113	0.551	0.018*
Internal validation set	0.030*	0.289	0.038*
External validation set	0.269	0.817	0.044*

* P <0.05 is considered to indicate statistical significance.

SUPPLEMENTAL FILES:

Online Supplemental Data: Results of univariate regression between clinical factors and CT signs in the training cohort

Factors	Training set		*P value*
	HT(n=50)	non-HT(n=59)	
Preoperative clinical factors			
Age, years	66.58±1.72	61.68±1.98	0.064
Sex, male	31(62%)	35(59%)	0.776
PLT(10^9/L)	166.78±7.90	199.64±8.43	0.006*
PT(s)	13.60(12.80-14.10)	13.60(12.80-14.43)	0.557
TT(s)	16.70(15.70-18.30)	17.60(16.20-18.73)	0.210
AT-III(%)	95.00(83.10-104.00)	89.00(79.75-98.88)	0.135
APTT(s)	33.40(27.70-36.20)	31.75(27.30-36.13)	0.529
D-D(μg/ml)	1.06(0.59-2.81)	1.37(0.72-4.16)	0.047*
FIB(g/L)	2.97(2.65-3.52)	2.85(2.33-3.50)	0.213
INR	1.07(1.01-1.14)	1.10(1.02-1.18)	0.353
LDL(mmol/L)	2.55±0.13	2.73±0.08	0.227
TC(mmol/L)	4.15±0.16	4.46±0.09	0.099
TG(mmol/L)	1.11(0.87-1.57)	0.89(0.76-1.16)	0.041*
History of hypertension	34(68%)	36(61%)	0.449
History of smoking	19(38%)	22(37%)	0.939
History of alcohol	12(24%)	16(27%)	0.710
History of cerebral infarction	12(24%)	7(12%)	0.096
History of cerebral hemorrhage	1(2%)	3(5%)	0.623
Embolism of cardiac origin	32(64%)	24(41%)	0.015*
Intravenous thrombolysis	12(24%)	15(25%)	0.864
Anticoagulant Therapy	4(8%)	2(3%)	0.410
SBP(mmHg)	132.00(125.00-149.00)	136.00(122.75-152.25)	0.561

Glu(mmol/L)	6.29(5.40-7.87)	7.75(6.77-11.39)	0.000*
GCS	13(11-15)	12(9-14)	0.165
NIHSS	17.38±0.63	15.56±0.55	0.032*
DPT(min)	280.00(240.00-360.00)	240.00(200.00-312.50)	0.009*
Intraoperative clinical factors			
Location of MT (Anterior circulation)	45(90%)	56(95%)	0.466
Times	2(1-3)	2(1-3)	0.156
Stent	3(6%)	12(20%)	0.048*
mTICI(≥2b)	46(92%)	58(98%)	0.177
CT signs			
Location of HDA (Basal ganglia)	43(86%)	54(92%)	0.358
Maximum CT value (HU)	86.00(73.00-110.00)	86.00(76.00-110.25)	0.770
Mean CT value (HU)	56.00(49.00-68.00)	58.50(47.75-68.25)	0.956
$Area_{max}$ (mm^2)	459.50(336.25-876.75.00)	250.00(136.00-392.00)	0.000*
High-density lesions in the subarachnoid space	35(70%)	26(44%)	0.007*
Mass effect	19(38%)	4(7%)	0.000*
Low density edema zone	14(28%)	6(10%)	0.017*
Low density mixed sign	39(78%)	30(51%)	0.003*
Metallic hyperdensity sign	24(48%)	24(41%)	0.443

*PLT: platelet, PT: prothrombin time, TT: thrombin time, AT-III: antithrombin-III, APTT: activated partial thromboplastin time, D-D: D-dimer, FIB: fibrinogen, INR: international normalized ratio, LDL: low-density lipoprotein, TC: total cholesterol, TG: triglyceride, SBP: systolic blood pressure, Glu: glucose, GCS: Glasgow Coma Scale, NIHSS: National Institutes of Health Stroke Scale, DPT: door-to-puncture, mTICI: Mechanical Thrombectomy in Cerebral Infarction, $Area_{max}$: the maximum cross-sectional area. P <0.05 is considered to indicate statistical significance.

Online Supplemental Data: Diagnostic performance of the three models

Models	Training set					Internal validation set					External validation set				
	AUC	Brier	SEN	SPE	ACC	AUC	Brier	SEN	SPE	ACC	AUC	Brier	SEN	SPE	ACC
Clinical factors& CT signs model	0.831	0.166	0.76	0.76	0.76	0.744	0.209	0.53	0.93	0.77	0.684	0.200	0.66	0.75	0.68
Glu	0.712	-	0.80	0.56	0.67	0.667	-	0.42	0.86	0.68	0.709	-	0.85	0.55	0.88
$Area_{max}$	0.792	-	0.58	0.88	0.74	0.713	-	0.42	0.93	0.72	0.642	-	0.57	0.81	0.64

Radiomics model	0.887	0.136	0.80	0.88	0.84	0.898	0.140	0.95	0.86	0.89	0.798	0.138	0.83	0.75	0.81
S(0,4)SumAverg	0.860	-	0.78	0.81	0.80	0.848	-	0.90	0.75	0.81	0.689	-	0.98	0.44	0.84
45dgr_GLevNonU	0.869	-	0.80	0.85	0.83	0.855	-	0.90	0.79	0.83	0.776	-	0.80	0.69	0.77
Combined model	0.895	0.126	0.78	0.88	0.84	0.882	0.144	0.95	0.79	0.85	0.820	0.132	0.81	0.81	0.81